Enhanced photopromoted electron transfer over a bilayer WO₃ n-n heterojunction prepared by RF diode sputtering

Gian Luca Chiarello[a]*, Massimo Bernareggi[a], Matteo Pedroni[b], Mirko Magni [a], Silvia M. Pietralunga[d,e], Alberto Tagliaferri[c,d], Espedito Vassallo[b], Elena Selli[a]

[a] *Dipartimento di Chimica, Università degli Studi di Milano, via Golgi 19, 20133 Milano, Italy*
[b] *CNR, Istituto di Fisica del Plasma "P. Caldirola", Via Roberto Cozzi 53, 20125 Milano, Italy*
[c] *Dipartimento di Fisica, Politecnico di Milano, P.zza Leonardo da Vinci 32, 20133 Milano, Italy*
[d] *CNST-IIT, via Pascoli 70/3, 20133 Milano, Italy*
[e] *CNR, Istituto di Fotonica e Nanotecnologie, P.zza Leonardo da Vinci 32, 20133 Milano, Italy*

Abstract

A bilayer WO₃ photoelectrode was obtained by radio frequency (RF) plasma sputtering in reactive 40%O₂/Ar atmosphere by depositing on a tungsten foil two successive WO₃ coatings at two different total gas pressures (3 Pa and 1.7 Pa, respectively), followed by calcination at 600 °C. Two monolayer samples deposited at each of the two pressures and a bilayer sample deposited at inverted pressures were also prepared. Their photoelectrocatalytic (PEC) activity was evaluated by both Incident Photon-to-Current Efficiency (IPCE) measurements and separate evolution of H₂ and O₂ by water splitting in a two-compartment PEC cell. SEM analysis revealed that the photoanodes have a nanostructured porous double layer surmounting a columnar basement (Staffa-like morphology, after the name of the Scottish island). Mott-Schottky analysis showed that the single layer deposited at 3 Pa has a conduction flat band potential 0.1 V more positive than that deposited at 1.7 Pa. The equivalent n-n heterojunction at the interface of the double-layer creates a built-in electric field that facilitates the photopromoted electron transfer toward the lower laying conduction band material, while the columnar innermost layer introduces percolation paths for efficient electron transport toward the conductive tungsten foil. Both phenomena contribute to decrease the interfacial charge transfer resistance (R_{ct}) and lead up to a *ca.* 30% increase in the PEC performance compared to the monolayer and to the inverted bilayer coatings and to a 93% faradaic efficiency, which is among the highest reported so far for WO₃ photoanodes. Upon methanol addition an outstanding 4-fold photocurrent density increase up to 6.3 mA cm^{-2} was attained over the bilayer WO₃ photoanode, much larger than the usually observed current doubling effect.

KEYWORDS: WO₃ photoanode; n-n heterojunction; RF sputtering, photocatalytic water splitting; photoelectrochemical cell; hydrogen production.

1. Introduction

The Paris climate change conference (COP21) sets out a worldwide agreement to keep global warming to less than 2 °C compared to pre-industrial levels. To achieve this ambitious goal, the agreement calls for zero net anthropogenic greenhouse gas emissions, including carbon dioxide, to be reached during the second half of this century. Hydrogen economy represents a possible solution to maintain the world energy demand, meanwhile pursuing the target of zero carbon emission from fossil fuels exploitation. Photocatalytic cleavage of water has been widely investigated as an environmentally-friendly method for renewable solar fuel production.[1–4] Separate streams of pure hydrogen and oxygen can be effectively obtained from water, using photoelectrocatalytic (PEC) cells.[4–7] In this technology, photoelectrodes made by thin coatings of suitable semiconductor materials harvest solar energy by absorbing photons with energy equal to or higher than the semiconductor band gap. The photogenerated charge carriers (electron-hole pairs) can promote thermodynamically up-hill reactions such as water splitting. In the case of n-type semiconductors, the material acts as photoanode for water oxidation to O_2, whereas the photopromoted electrons flow to the counter electrode where H_2 evolution takes place. One major issue in this process, which may seriously affect its efficiency, is the high probability of electron-hole pairs recombination.

Among suitable semiconductor photocatalysts, WO_3 has received much attention as an alternative to TiO_2[8,9] in consideration of its narrower band gap, ranging from 2.6 to 2.8 eV compared to 3.0 - 3.2 eV of TiO_2.[10,11] Thus, WO_3 can absorb up to 480 nm and be activated by visible light. However, the main drawback of WO_3 is that its conduction band (CB) potential is more positive than that of the H^+/H_2 couple. Hence, the electrons photopromoted in the WO_3 CB are not able to reduce protons to H_2 and this reaction needs to be boosted by an external applied voltage bias.

A multiple-layer strategy has often been investigated to improve the efficiency of photoactive materials. In the case of WO_3 several heterostructures have been studied, including WO_3/TiO_2,[12] $WO_3/BiVO_4$,[13] WO_3/Sb_2S_3[14] and WO_3/Cu_2O.[15] An effective charge carrier separation at the obtained heterojunction can be attained because both the CB and the valence band (VB) of all coupled semiconductors are located at higher energy than those of WO_3.[16] Kim *et al* also showed that the PEC performance of WO_3 can be improved by deposition of a thin alumina overlayer leading to a decrease of electron trapping sites on the WO_3 surface.[17] Enhanced photocurrent generation was recently attained with a triple-layered WO_3 photoanode grown by electrochemical anodization and attributed to the unique morphology of the material.[18]

Among the methods for thin films deposition, radio frequency (RF) plasma sputtering[19] proved to be very effective for the synthesis of photoactive coatings,[7,20–23] particularly because it enables to tune their properties through a precise control of the deposition parameters (RF power, total pressure inside

the chamber, composition of the gas atmosphere, deposition time, temperature and distance of the substrate). Moreover, this technique is already available for deposition of large surfaces and industrial scale production (*e.g.*, roll-to-roll sputtering). In a previous work,[24] some of us studied the effect of sputter oxygen partial pressure on the characteristics of the resulting WO_3 coatings and found that samples deposited in a 40%O_2/Ar atmosphere gave the most promising PEC performance. Moreover, WO_3 deposition at alternatively high and low gas pressures can minimize the well-known stress phenomena.[25] In this way, a more dense outermost layer grown at lower pressure relieves the stress to an underlying less dense one, resulting in larger critical thickness and good adhesion.[26] In particular, we found that the optimal high and low pressures were around 3 Pa and 1.5 Pa, respectively.[24]

In this work, we demonstrate that the electronic properties and the PEC performance of WO_3-based photoanodes can be tuned by changing the total pressure during the RF plasma sputtering deposition. In particular, the deposition of two successive layers of the same oxide sputtered at different pressure provides an effective route to obtain a n-n heterojunction bilayer system with good stability and enhanced PEC performance in terms of photocurrent generation, hydrogen production and faradaic efficiency.

2. Experimental procedure

2.1 Photoanodes preparation

Three WO_3 photoanodes were prepared by RF (13.56 MHz) plasma sputtering[19,24,27] in diode configuration at 140 W power and 1500 V of DC self-bias voltage. The WO_3 films were deposited on a tungsten foil (FB-Tecno, temper annealed, purity 99.6 %, 2 x 2 cm^2, and 0.2 mm thick), placed at 4.5 cm from the metal tungsten target in a reactive 40%O_2/Ar environment. The vacuum chamber was evacuated to less than 10^{-6} mbar before deposition. Two single layer coatings, labelled 1L(1.7Pa) and 1L(3Pa), were deposited at constant gas pressure of 1.7 Pa and 3 Pa, respectively. A double layer coating, labelled 2L(3+1.7Pa), was prepared by growing WO_3 at two different gas pressures, by first depositing at 3 Pa, followed by deposition at 1.7 Pa. Details on the deposition times, chosen as to achieve a *ca*. 1 μm thick photoactive layer in the three photoelectrodes, are reported in Table 1. The photoelectrodes were then calcined in oven at 600 °C for 2 h. Finally, two more photoanodes were prepared for comparison, *i.e.* a bilayer photoanode obtained by inverting the sequence of deposition pressures, followed by calcination at 600 °C, and labelled 2L(1.7+3Pa), and a compact dense WO_3 film, labelled 1L_calc, obtained by oxidation of the pristine tungsten foil surface in air at 600 °C for 2 h.

2.2 Photoanodes characterization

X-ray diffraction patterns were recorded on a Philips PW3020 powder diffractometer operating at 40 kV voltage and 40 mA current, by using the Cu Kα radiation (λ = 1.5418 Å). The patterns were compared with the Inorganic Crystal Structure Database (ICSD) data for phase identification. The film morphology, both at the surface and in cross-section, was investigated by High-Resolution Scanning Electron Microscope (SEM) imaging using a Tescan MIRA3 FESEM. X-ray photoelectron spectroscopy (XPS) measurements were performed with a Surface Sciences Instruments (SSI) M-Probe apparatus using Al Kα radiation (1486.6 eV). For all samples, the C 1s peak at 284.6 eV due to adventitious carbon was taken as the internal reference. UV-Vis-NIR diffuse reflectance spectra were recorded in the 220 - 2600 nm range with a Shimadzu UV3600 Plus spectrophotometer equipped with an ISR-603 integrating sphere. Photoluminescence spectra were recorded with an Edinburgh FLS980 spectrofluorimeter in the 360-650 nm range, upon excitation at 350 nm.

2.3 Electrochemical measurements

Electrochemical measurements were performed in a two-compartment three-electrode PEC cell filled with a 0.5 M sodium sulphate solution. The sputtered WO_3/W electrode acted as working electrode (9.6 cm^2 geometric area), a platinum wire (bent into a three loops coil) was the counter electrode and an aqueous saturated calomel electrode (SCE) was the reference. All measurements were performed with a Metrohm Autolab PGSTAT302N potentiostat/galvanostat equipped with a frequency response analyzer module (FRA32M) for electrochemical impedance spectroscopy (EIS).

The electrochemical surface area (ECSA) of each sputtered tungsten oxide electrode was estimated by recording three consecutive potential cycles centred around the open circuit potential (OCP), sweeping between -0.15 and -0.05 V $vs.$ SCE at scan rates from 0.025 to 0.3 V s^{-1}. The capacitive currents evaluated in the middle of the range were then plotted as a function of the sweep rate potential.[28,29]

The flat band potential, E_{FB}, and the density of donors, N_D, of the investigated semiconducting WO_3 photoanodes were evaluated by Mott-Schottky (MS) analysis.[30] Measurements were performed in the dark and in 0.5 M Na_2SO_4 N_2-purged solution, recording impedance spectra (30 frequency values, single sine, logarithmically distributed from 10^4 Hz to 0.03 Hz, 0.01 V amplitude) at a constant applied potential ranging from 0.1 to 1.0 V $vs.$ SHE (the experimental applied potential $vs.$ SCE was converted to SHE by adding 0.244 V). The oxide film was first conditioned at 0 V $vs.$ SCE for 30 s and then at the selected potential for 30 s. During the entire EIS test a flux of N_2 was maintained at the surface of the solution. Considering the frequency dispersion of the resulting MS analysis,[31] the EIS spectra were fitted with a Randles-type equivalent circuit $R_s(R_pQ)$, where R_s is the serial

4

resistance, R_p the polarization resistance and Q a constant-phase element. Q substitutes the common capacitor, and allows one to calculate the effective capacitance C, to draw $1/C^2$ *vs.* applied potential plots.[32]

EIS spectra were also measured under working condition for hydrogen production, *i.e.* under irradiation (19.7 mW cm^{-2}) and at 1.0 V *vs.* SCE bias, by sampling sixty frequencies (single sine logarithmically distributed from 10^5 Hz to 0.1 Hz, 0.01 V amplitude). Data were fitted with the aforementioned modified Randles equivalent circuit, where R_{ct} instead of R_p stands for the charge transfer resistance associated to photo-assisted water oxidation reactions occurring at the WO$_3$ surface. All EIS spectra were fitted using the Z-View software (Scribner Associates, Inc.).

2.4 IPCE measurements

The incident photon to current efficiency (IPCE) was measured on an optical bench already described elsewhere,[33] including a 300 W Xe lamp (Lot-Oriel), a monochromator (LOT-Oriel Omni-λ 150), a shutter (Thorlabs SC10), a calibrated photodiode (Thorlabs S130VC) connected to a power meter (Thorlabs PM200), and a potentiostat/galvanostat (Amel, mod. 2549). Measurements were done in the three-electrode PEC cell, biased at 1.0 V *vs.* SCE in 0.5 M Na$_2$SO$_4$ electrolyte solution. The percent IPCE at each wavelength λ was calculated as:

$$\% \, IPCE = \frac{i_\lambda}{P_\lambda} \cdot \frac{1240}{\lambda} \cdot 100 \qquad (1)$$

where i_λ is the photocurrent density (mA cm^{-2}) at a specific incident λ (nm), P_λ is the incident power density (mW cm^{-2}) at the same λ, and 1240 (J nm C^{-1}) = $h \, c \, q^{-1}$, h being the Planck constant, c the speed of light and q the charge of a single electron.

2.5 Photocatalytic water splitting tests

Photocatalytic water splitting tests were conducted in the above described two-compartment PEC cell. The three electrodes were immersed in a 0.5 M Na$_2$SO$_4$ electrolyte solution and connected to an Amel, mod. 2549 potentiostat/galvanostat for photocurrent measurements while applying 1 V *vs.* SCE external potential bias. The photoanode was illuminated through a Pyrex glass optical window employing an iron halide mercury arc lamp (Jelosil HG200, 250 W) as irradiation source, emitting in the 350 - 450 nm range with an incident power density of 19.7 mW cm^{-2} (emission spectrum in Fig. S1 of the Electronic Supporting Information). The evolved H$_2$ and O$_2$ gases were collected into two graduated burettes surmounting the two compartments of the cell, which were initially filled with the electrolyte solution.[6] The volume of produced gas was measured every 60 min by the displacement

of the liquid in the burettes, after shuttering the light. Each photoanode was tested for at least 6 h-long irradiation.

3. Results and discussion

3.1 Photoanode characterisation

3.1.1 XRD analysis

The as grown films, deposited at room temperature, are notoriously amorphous.[24] As shown in Fig. 1, all sputtered WO_3 coatings after calcination at 600 °C exhibit diffraction patterns similar to those of the oxidized tungsten foil surface (sample 1L_calc). The crystal structure of WO_3 consists of corner-sharing octahedrals (Fig. S2). Because several distortions are possible, WO_3 can exist in many different polymorphs depending on the annealing temperature, *i.e.* triclinic from −50 to 17 °C,[34] monoclinic up to 330 °C, orthorhombic up to 740 °C, and tetragonal above 740 °C.[35] Monoclinic and orthorhombic structures have similar XRD patterns (see the bottom of Fig. 1). Thus, it is not simple to discern between these two phases, also because of the XRD peak broadening and shift, due to possible distortions originated by oxygen vacancies. Nevertheless, because of the high annealing temperature, our sputtered WO_3 coatings are expected to have a distorted orthorhombic structure. Moreover, the relative intensity of the diffraction peaks significantly differs from that of the reference, the most intense peaks being those located at $2\theta = 23.5°$ and 48.1° corresponding to the parallel (020) and (040) planes (Fig. S2). This indicates a preferred orientation along the [010] direction, as often occurs in thin films and metals.[36] Noteworthy, films grown on (100) silicon wafers under the same operation conditions and reported in our previous work[24] showed the opposite preferred orientation, the peak centred at $2\theta = 23.5°$ being the weakest one. Because the metal tungsten foil support also exhibits a preferred orientation (Fig. S3), one may conclude that the sputtered coating follows a nearly epitaxial growth (and spatial rearrangement) process, with the crystallographic axes of the deposited layer aligning along the orientation of the support underneath.

3.1.2 SEM analysis

SEM investigation of the pristine metal tungsten support (Fig. 2A and S3C) confirms the layered microstructure responsible for the preferred crystallographic orientation. After annealing at 600 °C for 2 h in air, the tungsten foil surface underwent oxidation forming a compact 1.5 μm thick WO_3 layer (sample 1L_calc, see Fig. 2B). Interestingly, the cross-section SEM images of the annealed 1L(1.7Pa) and 1L(3Pa) samples (Fig. 2C and D) reveal the presence of a 2.3 μm thick WO_3 film possessing a hierarchical structure with a porous layer surmounting a columnar basement. This morphology resembles that of the cliffs in the Isle of Staffa (Pillar Island) of volcanic origin in the

6

west of Scotland. The WO$_3$ film was much thicker than expected on the basis of the sputtering deposition rate. However, the cross-section image of the as grown 2L(3+1.7Pa) sample (*i.e.,* before annealing, Fig. 2E) shows that the initial double-layer lying over the smooth tungsten metal surface is *ca.* 1 μm thick, as expected. After annealing at 600 °C in air (Fig. 2F) the film thickness increases to 2.3 μm due to the formation of the columnar basement. Hence, the innermost WO$_3$ vertically aligned array is formed upon oxidation of the metal tungsten surface in contact with the sputtered coating. However, the resulting ordered morphology differs from that observed after calcination of the bare tungsten foil (Fig. 2B), suggesting that the formation of this ordered structure is driven by the presence of the porous sputtered coating above. Thus, the calcined 2L(3+1.7Pa) sample exhibits a Staffa-like morphology (Fig. 2G), actually consisting of *i*) a porous double-layer grown by RF diode sputtering (Fig. 2H), and *ii*) an underneath columnar layer formed by surface oxidation of the tungsten support during calcination in the presence of the overlaying sputtered oxide.

3.1.3 Electrochemical surface area

The electrochemically active surface area (ECSA) gives an estimation of the real surface area involved in photoelectrochemical processes. It can be estimated by the potential scan-rate dependence of the capacitive current due to the double-layer charging and discharging at the solid-electrolyte interface.[28,37] The non-faradaic region of the cyclic voltammograms is typically a range of few tens of millivolts centred around the open-circuit potential, OCP. In this potential region the capacitive current (I_c) is linearly dependent on the scan-rate v according to $I_c = \text{ECSA} \cdot C_s \cdot v$, where C_s is the intrinsic specific capacitance. The ECSA$\cdot C_s$ product, corresponding to the double-layer capacitance C_{DL} of the interface, can be determined by the slope of the straight line interpolating I_c as a function of v, taken at the central potential of the cyclic voltammograms during both the anodic and cathodic scan (Fig. S5). The value of C_s depends on the nature of the semiconductor material and of the electrolyte. Typical values are in the 15−130 μF cm^{-2} range.[37] However, in the absence of a reference electrode of known ECSA, a reasonable value of $C_s = 60$ μF cm^{-2} for metal oxides[38] can be used to estimate the surface area of the investigated electrodes. Table 1 shows that the compact 1L_calc sample has an ECSA close to its geometric surface area, A_g (14.5 cm^2 *vs.* 9.6 cm^2, 3.5 cm being the diameter of electrode), resulting in a roughness factor, $r_f = \text{ECSA} / A_g$, of 1.5. In contrast, the porous sputtered coatings possess much larger surface area and, accordingly, much higher r_f. The ECSA of the film deposited at higher pressure (3 Pa) is 17% larger than the ECSA of the film deposited at lower pressure (1.7 Pa). Indeed, at higher pressure the sputtered tungsten atoms undergo more frequent collisions with energy transfer (*i.e.* energy loss) to the background gas before reaching the substrate. This results in a lower atom mobility and in a variation of the atomic arrangement of the

7

deposited film, with the formation of a less dense, more porous coating with larger surface area. As expected, 2L(3+1.7Pa) and 2L(1.7+3Pa), being deposited at both pressures, have a surface area intermediate between those of 1L(3Pa) and 1L(1.7Pa).

3.1.4 Band gap structure

The UV-vis-NIR diffuse reflectance spectra (DRS) are presented in Fig. 3 as Tauc-plots of the Kubelka-Munk transform, $F(K)=(1-R)^2/2R$, for direct allowed transitions. The spectra show oscillations in the visible region typical of thin films, originated by the interference of the waves reflected at the top and bottom surface of the film. Their frequency and amplitude depend on the film thickness d.[33] The d values of the calcined sputtered coatings, calculated using a dedicated tool of the spectrophotometer software, are collected in Table 1. Interestingly, the results are in good agreement with the thickness of the outermost sputtered layer (*ca.* 1 μm), indicating a partial reflectance of light at the porous-columnar interface. By contrast, the dense 1L_calc sample shows no interference fringes, indicating that its thickness exceeds the light penetration depth.

The band gap energy E_g can be obtained by the Tauc plot, $(F(K)h\nu)^{1/2}$ *vs.* hν, at the intersection between the linear region of the absorption edge and the linear fit of the background at lower energy (Fig. 3). The band gap absorption threshold of all samples is located above 2.8 eV (*ca.* 440 nm). In particular, the 1L(1.7Pa) coating exhibits a 0.11 eV wider E_g with respect to that of 1L(3Pa) (Table 1). A variation of WO_3 band gap from 3.2 eV to 2.5 eV as a function of both deposition pressure and temperature is widely documented in the literature.[39–42]

In order to better understand the origin of the difference in the band gap of 1L(3Pa) and 1L(1.7Pa), we estimated the position of the CB using the Mott-Schottky equation (Eq. 2). In this model, the CB edge is measured as flat band potential E_{FB}, *i.e.* the voltage at which the potential drop in the space-charge layer is zero and the semiconductor bands are flat. For n-type semiconductors:

$$\frac{1}{C_{SC}^2} = \frac{2}{\varepsilon\varepsilon_0 q N_D}\left(E_{appl} - E_{FB} - \frac{kT}{q}\right) \qquad (2)$$

where C_{sc} is the space-charge capacity of the semiconductor, E_{appl} the applied bias voltage, ε the dielectric constant of the semiconductor (35.2 for WO_3),[43] ε_0 the permittivity of vacuum (8.85 10^{-14} F cm^{-1}), N_D the donor dopant density, q the elementary charge, k the Boltzmann constant and T the absolute temperature. E_{FB}, at a given T and pH of the electrolyte solution, can be obtained by extrapolating to zero the linear part of the C^{-2} *vs.* E_{appl} plot (Fig. 4), where $E_{FB} = E_{appl}(C^{-2} = 0) - kT/q$, whereas N_D can be calculated directly from the slope. The results presented in Table 1 show that 1L(1.7Pa) has a E_{FB} shifted of 0.1 V towards more negative potentials (*i.e.,* higher energy) with respect to 1L(3Pa). Thus, the wider band gap of the coating prepared at lower pressure is due to the

up-shifting of the CB energy. XPS valence band spectra (Fig. 5) further confirm this finding showing that both monolayer samples have the E_{VB} located at the same energy (3.0 eV) with respect to the Fermi level, E_F.

The negative slope of the Mott-Schottky plot confirms the n-type character of the synthesized semiconductor coatings due to the presence of oxygen vacancies, in the form of W^{5+} or W^{4+} sites, acting as electron donors. Their optical transition energy level is typically located 0.77–1.0 eV below the CB minimum.[44] The density of donor species N_D calculated from the slope of the Mott-Schottky plot (Table 1) demonstrates that the coating prepared at lower pressure has a larger N_D, *i.e.* more oxygen vacancies, in agreement with the reactive sputtering process. In fact, a higher gas pressure in the deposition chamber during the deposition process leads to an increased probability that evaporated W atoms react with O_2 molecules, with a consequent lower amount of oxygen vacancies in the sputtered WO_3 layer. According to DFT calculations, the highest energy valence levels of WO_3 are predominantly O 2p states, whereas the bottom of the CB is mainly composed of W 5d states partly mixed with O 2p orbitals.[45–47] These studies also predict, based on the crystal field theory (CFT), that a distortion of the WO_6 octahedron and in particular a change in W–O bond length can affect the position of the CB bottom.[45] Hence, the variation of the CB position as a function of the sputtering total pressure can tentatively be attributed to the different extent of crystal distortion induced by the different oxygen vacancy content.

The different band gap and doping levels measured in the two coatings prepared at the two deposition pressures suggest that in the 2L(3+1.7Pa) sample an equivalent n-type to n-type heterojunction is created at the interface between the two WO_3 layers. Interestingly the 2L(3+1.7Pa) sample has a E_{FB} value intermediate to those of single layer 1L(3Pa) and 1L(1.7Pa), and a much lower equivalent density of donors. Indeed, the bilayer sample can be modelled as two capacitors connected in series. Because the density of charge of each capacitor is equal to $\rho = N_D\, q$, where N_D is that of each single layer calculated from the Mott-Schottky equation ($N_{D,1.7Pa} = 1.58 \cdot 10^{20}$ cm^{-3} and $N_{D,3Pa} = 1.34 \cdot 10^{20}$ cm^{-3}), and q the unitary charge, then the equivalent charge density ρ_{eq} of the bilayer is:

$$\rho_{eq} = \left(\frac{1}{\rho_{1.7Pa}} + \frac{1}{\rho_{3Pa}}\right)^{-1} = 0.72 \cdot 10^{20} \text{ C cm}^{-3} \qquad (3)$$

The N_D value of the so modelled bilayer is very close to the measured one ($0.80 \cdot 10^{20}$ C cm^{-3}). Thus, both E_{FB} and N_D values obtained for 2L(3+1.7Pa) by the Mott-Schottky plot give experimental evidence supporting the formation of a n-n heterojunction.

3.1.5 Photoluminescence and X-ray photoelectron spectroscopies

Photoluminescence (PL) spectroscopy[42,48,49] and theoretical calculations[44,46,47,50] have been widely employed to ascertain the nature of defects in WO_3. The PL emission spectra of the WO_3 sputtered coatings recorded under excitation at 350 nm are shown in Fig. 6. These spectra can be reasonably deconvoluted into four Gaussian curves (Fig. S6) centered at *ca.* 410, 440, 490 and 550 nm. The first emission band, occurring at energy greater than the band gap, has been attributed to the direct recombination of "hot electrons" which have not fully relaxed to the bottom of the CB.[49] The second and most intense band is originated by the recombination of free charge carriers from the bottom of the CB to the VB (band-to-band recombination). The emission at energy lower than the E_g necessarily involves infra band gap energy states of donors trapped in either surface or bulk defects. In the case of WO_3, the removal of an O atom from the –W–O–W– lattice chain may lead to the formation of different charge states (0, 1+, 2+) of oxygen vacancies (V_O) in the form ($W^{5+}/V_O^0/W^{5+}$), ($W^{4+}/V_O^0/W^{6+}$). ($W^{5+}/V_O^+/W^{6+}$), and ($W^{6+}/V_O^{2+}/W^{6+}$).[44,51] By applying hybrid density functional calculations, Wang *et al.* [44,52] reported that the energy levels describing the possible PL transitions involving these charge states are all located in the band gap and can be associated with the radiative decay of electrons from the vacancy states (V_O^0 or V_O^+) to the VB, according to:

$$V_O^0 \rightarrow V_O^+ + e_{VB}^- + h\nu \qquad (4)$$

$$V_O^+ \rightarrow V_O^{2+} + e_{VB}^- + h\nu \qquad (5)$$
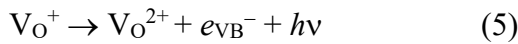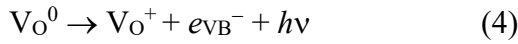
Because the energy level of V_O^0 is predicted to be closer to the CB than the V_O^+ level, the PL emission bands at *ca.* 490 nm (2.53 eV) and 550 nm (2.21 eV) can be attributed to transition (4) and (5), respectively. Finally, the band at 560 nm, that appears more intense in the case of 2L(3+1.7Pa), can be tentatively attributed to a localized increase of V_O^+ levels due to the formation of a depletion layer at the heterojunction, consequent to band alignment at the interface.

The presence of W^{5+} was confirmed by XPS analysis (Fig. 7 and Fig. S7). Indeed, the XPS spectra in the W 4f binding energy region (Fig. 7a) of all coatings were fitted as the convolution of two W $4f_{7/2}$–W $4f_{5/2}$ doublets, with the main peaks centered at 34.7 eV and 35.9 eV, originated from W^{5+} and W^{6+}, respectively. The spin–orbit spacing and the area ratio of both doublets were constrained to 2.18 eV and 4:3, respectively.[53,54] The oxygen 1s region (Fig. 7b) shows a main peak located at 530.5 eV, due to structural oxygen in WO_3, and a minor one at 532 eV, assigned to oxygen in surface hydroxyl groups (or adsorbed water). The elemental analysis (Table 2) shows that in all samples the O:W atomic ratio is under stoichiometric. The 1L(1.7Pa) sample possesses a lower O:W atomic ratio (*i.e.* more O vacancies) than 1L(3Pa), in line with the larger density of donors N_D calculated from the Mott-Schottky plot.

3.2 PEC results

3.2.1 IPCE

All IPCE curves of the investigated photoanodes exhibit an activity onset below 450 nm in agreement with the calculated E_g from the UV-vis DRS spectra. The IPCE curves recorded under hydrogen evolution conditions (1.0 V *vs.* SCE and pH 7) confirm the narrower band gap of the coating deposited at higher pressure (Fig. S8). Moreover, 1L(3Pa) shows a slightly higher efficiency than 1L(1.7Pa), likely due to its larger surface area (Table 1). The efficiency of the 2L(3+1.7Pa) photoanode is significantly higher than those of the single layer photoanodes, despite the similar surface area and photoactive film thickness (Fig. 8). Noteworthy, the IPCE considerably increases after the PEC water splitting test (*i.e.*, after 6 h-long irradiation) and the maximum efficiency shifts towards longer wavelengths, *i.e.* from 330 nm to 360 nm. This phenomenon is very likely due to the decrease of the oxygen vacancies (*i.e.*, crystal defects) occurring during irradiation, which can act as electron-hole pairs recombination centres (see section 3.2.3.).

3.2.2 Polarization curves

Fig. 9 shows the polarization curves from −0.1 V to 1.6 V *vs.* SCE range, performed over the compact 1L_calc (Fig. 9a) and 2L(3+1.7Pa) (Fig. 9b) photoanodes, either under continuous or chopped irradiation. The photocurrent potential onset above 0.05 V (*i.e.,* 0.29 *vs.* SHE) is in agreement with the flat band potential calculated from the Mott-Schottky plot. Two main differences can be noticed by comparing Fig. 9a and 9b: *i*) under continuous irradiation the porous double-layer sputtered WO$_3$ photoanode reaches a saturated photocurrent density of 1.6 mA cm^{-2} at *ca.* 0.8 V; *ii*) the photocurrent recorded under chopped light with 2L(3+1.7Pa) significantly exceeds that measured under continuous irradiation. In contrast, the compact 1L_calc photoanode generates a lower photocurrent that continuously increases without reaching saturation, and the photocurrent under chopped light matches that measured under continuous irradiation.

The superior photoactivity of porous WO$_3$ films with respect to compact ones has already been reported.[1,11,55,56] Pros and cons can be recognized in nanostructured photoelectrodes. The advantages of porous coatings are: *i*) larger surface area providing more active sites for reactant adsorption and charge transfer; and *ii*) shorter carrier collection pathways to the surface, with a lower probability of electron-hole pairs recombination. Moreover, the shorter diffusion path requires a lower potential for extraction of bulk holes to the surface, allowing to reach the saturated photocurrent density over the porous film. On the other hand, the main disadvantage of nanocrystalline porous coatings is the slower charge transport by diffusion compared to the faster drift occurring in bulk films.[57,58] The additional barrier at the interparticle interface further hampers charge diffusion. Because electrons and holes under polarization migrate towards opposite directions, both phenomena increase the recombination

11

probability. This explains the moderately higher photocurrent density of porous photoanodes compared to the compact one, despite the more than one order of magnitude larger surface area (*ca.* 300 cm^2 for each porous electrode, see Table 1, to be compared with 14.5 cm^2 for the compact one). Finally, as expected by the IPCE curves, the 2L(3+1.7Pa) photoanode produces a 30% higher saturated photocurrent than the single layer coating (Fig. 9c), in spite of the similar film thickness and surface area. Noteworthy is also the lower saturated photocurrent value attained with the 2L(1.7+3Pa) inverted heterojunction, compared to the 2L(3+1.7Pa). Also in this case the net difference in photocurrent can not be attributed to a difference in the active area (280 cm^2 *vs.* 293 cm^2, respectively).

3.2.3 PEC water splitting results

The time on stream hydrogen and oxygen evolution and the photocurrent density recorded at 1.0 V *vs.* SCE and pH 7 during the photocatalytic water splitting tests are presented in Fig. 10 and Table 3. The photocurrent density significantly increased during the first irradiation hour over all fresh coatings, while steady state conditions (*i.e.,* stable photocurrent and linear gas evolution) were reached only after the second hour. During this transient period, which appears to be shorter for 2L(3+1.7Pa) than for the 1L photoelectrodes, the "extra current" is very likely generated by a photo-assisted partial oxidation of the highly defective WO$_{3-x}$ coating, such as:

$$(W^{5+}/V_O^0/W^{5+}) + H_2O \overset{h\nu}{\rightarrow} (W^{6+}–O–W^{6+}) + 2\ H^+ + 2\ e^- \qquad (6)$$
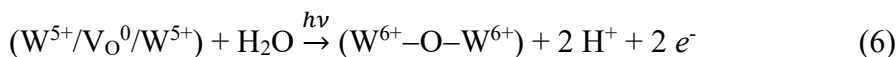
This hypothesis is corroborated by three experimental observations: *i*) the H$_2$ to O$_2$ molar ratio during this period is larger (*ca.* 2.6) than during the following stationary period (Table 2); *ii*) the intensity of the PL emission spectra recorded after the 6 h-long photocatalytic tests is considerably suppressed (see Fig. 6, dotted lines), accounting for a reduced number of oxygen vacancies as photoemission sites; and *iii*) the fresh photoanode exhibits a pronounced hydrophobic surface that turns hydrophilic after the 6 h-long irradiation test (Fig. S9). Photoinduced hydrophilicity is a well known phenomenon occurring on several metal oxides including WO$_3$. An increased wettability is related to an increase of surface energy due to filling surface oxygen vacancies with OH groups.[59]

After *ca.* two hours, both H$_2$ and O$_2$ evolved at constant rate under irradiation (pseudo zero order kinetics). Slightly higher H$_2$ and O$_2$ production rates (r_{H_2} and r_{O_2}, respectively) were obtained with 1L(3Pa) possessing a larger surface area than 1L(1.7Pa), while 2L(3+1.7Pa) outperforms single layer samples in terms of both r_{H_2} and H$_2$:O$_2$ mole ratio, that approaches the stoichiometric value of 2 (Table 3). Indeed, a very high (93%) faradaic efficiency η_F (*i.e.* the photocurrent-to-oxygen conversion efficiency)[17] was attained over this photoanode in comparison with the efficiency values reported in the literature for WO$_3$ thin films, usually ranging between 18% and– 80%.[17,29,60] The

larger H_2 to O_2 evolution rate with respect to stoichiometry is usually attributed to the side formation of H_2O_2.[17] In contrast, 2L(1.7+3Pa) with inverted heterojunction showed a less stable photocurrent profile along the 6-h irradiation test (Fig. 10b), a lower hydrogen production rate and a remarkably lower faradaic efficiency (80.8%) with respect to the most performing 2L(3+1.7Pa) photoanode.

Finally, Fig. 10b shows that the 2L(3+1.7Pa) photoanode also demonstrated a very high time stability, maintaining a stable photocurrent density along the 6 h continuous irradiation following the 5 h-long irradiation under shuttered conditions.

3.3 Electrochemical impedance measurements

The Nyquist plots recorded at 1.0 V *vs.* SCE, in 0.5 M Na_2SO_4 and under full lamp irradiation (Fig. 11) exhibit the typical semicircle shape, best fitted by a simplified Randles equivalent circuit $R_s(QR_{ct})$ (inset in Fig. 11). In this model, the electrochemical reaction is limited only by the surface-mediated electron transfer and not by reactant diffusion through the Helmholtz layer. From a qualitative point of view, the diameter of the semicircle is equal to the charge-transfer resistance (R_{ct}). Thus, the compact 1L_calc photoanode exhibits the greatest resistance, whereas best performing 2L(3+1.7Pa) exhibits the lowest resistance. The fitting results presented in Table 4 can be summarized as follows:

R_s is the series resistance accounting for all ohmic resistors (external contacts and wires, electrode sheet resistance) and the electrolyte resistance. As expected, similar values are obtained for all samples, though R_s is slightly higher for 2L(3+1.7Pa) and 2L(1.7+3Pa), tentatively due to the additional interface resistance between the two WO_3 sputtered layers.

Q is the constant phase element that takes into account the non-ideal behavior of the interface double layer. This pseudo-capacitance can be treated as at least two capacitors (the space-charge region C_{SC} and the Helmholtz double layer C_H) connected in series, $C^{-1} = C_{SC}^{-1} + C_H^{-1}$. The former capacitance is located at the semiconductor surface where the positive charges, in the form of ionized donors, attract the negative counter charges at the surface. This, in turn, attract the hydrated mobile ions of the electrolyte on the liquid side creating the inner (IHP) and the outer (OHP) Helmholtz plane. However, by considering the lower carrier density in semiconductors with respect to the electrolyte, it is possible to neglect the C_H term in the connection, so $C^{-1} \approx C_{SC}^{-1}$.

The capacitance depends on both the density of donor species (*i.e.,* the charges stored in the depletion layer) and on the geometry of the electrode. Table 4 shows that the compact photoanode (1L_calc) has one order of magnitude greater normalized capacitance per unit area (C_n) compared to the porous sputtered photoanodes. Indeed, the compact 1L_calc is a flat electrode (it can be modelled as parallel-plate capacitor) and it has a lower surface to volume ratio (*i.e.,* larger density of positive charges per unit surface area). In contrast, the porous film can be described, in first approximation,

as coaxial cylinders (to simulate the shape of pores) that notoriously have lower capacitance per unit surface than the parallel plates.

R_{ct} is the charge-transfer resistance associated to the oxidation reaction occurring at the semiconductor/electrolyte interface. R_{ct} is a very important parameter because it is inversely proportional to the rate constant of the half anodic reaction:

$$R_{ct} = \frac{\eta}{I_{ct}} = \frac{E_{appl} - E_{FB}}{n\,F\,r_{O_2}} \qquad (7)$$

where $\eta = (E_{appl} - E_{FB})$ is the potential drop in the space-charge layer, I_{ct} is the charge transfer current, n the number of electrons involved in the half reaction, F the Faraday constant, and r_{O_2} the oxygen evolution rate. The linear interpolation of R_{ct} vs. η/r_{O_2} of all investigated samples (Fig. S10) gives a slope of 2.55 x 10^{-6} mol C^{-1}, i.e. very close to the expected $(4 \cdot F)^{-1}$ = 2.59 x 10^{-6} mol C^{-1}, proving the validity of the attribution of R_{ct} parameter to the oxygen evolution reaction. Hence, a decrease of R_{ct} corresponds to an increase in I_{ct} and, therefore, in r_{O_2}. In photocatalytic water oxidation, the charge transfer current is due to the reaction of surface adsorbed water, or hydroxyl groups, with photogenerated VB holes. Table 4 shows that the two sputtered monolayer photoanodes have similar charge transfer resistance normalized per unit area, $R_{ct,n}$, whereas best performing 2L(3+1.7Pa) possesses a ca. 30% lower $R_{ct,n}$ in agreement with the 30% greater IPCE, r_{H_2} and generated saturated photocurrent density. Indeed, a larger density of VB holes induces a more effective surface reaction with the electron donor species with the consequent increase of the I_{ct} and decrease of charge transfer resistance (Eq. 7). This is confirmed by the significantly larger R_{ct} of the 2L(1.7+3Pa) inverted heterojunction with respect to that of 2L(3+1.7Pa) because this electronic configuration cannot benefit of the enhanced electron transfer. Nevertheless, the 0.1 eV difference between the CB at the interface of the inverted heterojunction introduces only a modest energy barrier to the electron transfer and in fact this sample shows an R_{ct} intermediate to those of the monolayer samples.

Finally, the EIS investigation demonstrates that the greater photocatalytic performance of the sputtered double layer photoanode can be ascribed to a larger density of reactive VB holes, due to a better photopromoted electrons transfer at the n-n heterojunction, as depicted in Scheme 1. Indeed, a larger density of VB holes induces a more effective surface reaction with the electron donor species with the consequent increase of the I_{ct} and decrease of R_{ct} (Eq. 7). Interestingly, 1L_calc exhibits a considerably lower $R_{ct,n}$. These results are in line with the pros and cons of compact to porous photoanodes: the compact photoanode possesses the higher intrinsic photocatalytic activity (i.e., the lower $R_{ct,n}$). However, the overall photoactivity compared to the porous films is hindered by the much lower surface area.

3.4 Effect of methanol addition

The photocurrent density profile measured during the photocatalytic water splitting tests (Fig. 10b and Fig. 12a) showed an abrupt increase as the light was turned on, generating a photocurrent peak, particularly intense on the 2L(3+1.7Pa) film, followed by a decrease up to a stationary photocurrent value which is almost common to all investigated photoanodes. By contrast, over the compact 1L_calc film the photocurrent density instantly reaches a stable value upon illumination. We ascribe the sharp photocurrent peak recorded with 2L(3+1.7Pa) to the fast photopromoted electron transfer at the n-n heterojunction consequent to the shift towards higher energy of the CB of the outer layer (Scheme 1). Conversely, the holes are not as much promptly transferred as the electrons because the VB of the two layers lie at the same level. Thus, the faster electron transfer at the beginning of irradiation leads to an increase of VB holes density, also due to a not equally fast holes re-filling by the reaction with the electron donor species. This causes, on one hand a reduced R_{ct} (*i.e.*, a higher faradaic efficiency), on the other hand a slight depletion of VB holes, that cannot sustain the initial high photocurrent, and an increased probability of charge carrier recombination. Both phenomena are responsible for the subsequent photocurrent drop. After the initial photocurrent spike, water oxidation at the photoanode surface is the rate-determining step of the whole process. The absence of the sharp peak over both the monolayer and the inverted heterojunction samples further corroborates this interpretation.

In order to further explore this phenomenon, an additional experiment were performed with all photoanodes upon addition of 1.2 M CH_3OH to the Na_2SO_4 aqueous solution (Fig. 9d-f and Fig.12b). In fact methanol is a more efficient hole scavenger than water. As a result, Fig. 12b shows that no photocurrent peak appears at the beginning of irradiation, and stable and considerably higher photocurrent density values are attained with all photoelectrodes. According to previous studies on WO_3 photoelectrodes (Table 5), a *ca.* 2-fold increase of photocurrent density is usually attained in the presence of methanol. Besides to the better ability of methanol to fill VB holes, this photocurrent density enhancement is notoriously due to the so called current doubling effect. It is interesting to notice that our reference 1L_calc sample also exhibits a 2.4-fold increase of photocurrent density upon methanol addition,. In contrast, 1L(3Pa), 1L(1.7Pa), and 2L(1.7+3Pa) produce similar photocurrent density around 3.9 mA cm^{-2}, *i.e.* a 3.5 times improvement in the presence of methanol. The most performing 2L(3+1.7Pa) achieves a photocurrent density of 6.3 mA cm^{-2}, which is *ca.* 4-fold the value attained in the absence of methanol. This unprecedented photocurrent increase proves that, in the case of this WO_3 n-n heterojunction-containing electrode, methanol not only has an efficient hole scavenging effect, but also boosts the effective charge carrier separation in the presence of current doubling. Moreover, the inverted heterojunction 2L(1.7+3Pa) sample shows a deactivation

along the irradiation time likely due to the lower stability of the coating, in line with our original multilayer deposition strategy, with a less dense layer underneath a denser one, to relieve the stress and increase the coating adhesion.

4. Conclusions

This work demonstrates that the total pressure during WO_3 deposition by RF diode sputtering affects the position of the CB energy very likely due to the different extent of crystal structure distortion induced by oxygen vacancies. Lowering the pressure increases the oxygen vacancies, and produces a shift of the CB towards higher energy. Thus, a WO_3/W bilayer photoanode possessing an equivalent n-n heterojunction has been successfully prepared by growing the two WO_3 layers at two different pressures, followed by calcination at 600 °C. The built-in electric field generated at the interface between the two WO_3 layers implies an improved photopromoted electron transfer along a downhill pathway in the CB level from the outer toward the inner layer. This leads to a decreased surface charge transfer resistance, to a stable photocurrent up to 12 hours and a 30% improvement of the PEC performance with respect to the corresponding single layer photoanodes. Because water oxidation at the photoanode surface is the rate determining step, the effect of the enhanced electron transfer at the heterojunction can be fully exploited only in presence of methanol, due to both more efficient hole scavenging and photocurrent doubling, up to an unprecedented stable 4-fould photocurrent increase. The bilayer formation strategy presented in this work might be extended to produce photoelectrodes based on any other semiconductor material with tuneable band gap energy, opening the way to a novel effective approach towards more efficient photoelectrochemical cells.

References

1   F. E. Osterloh, *Chem. Soc. Rev.*, 2013, **42**, 2294–320.

2   A. Kubacka, M. Fernández-García and G. Colón, *Chem. Rev.*, 2012, **112**, 1555–1614.

3   G. L. Chiarello and E. Selli, *Recent Patents Eng.*, 2010, **4**, 155–169.

4   B. D. Alexander, P. J. Kulesza, I. Rutkowska, R. Solarska and J. Augustynski, *J. Mater. Chem.*, 2008, **18**, 2298.

5   M. Grätzel, *Nature*, 2001, **414**, 338–344.

6   E. Selli, G. L. Chiarello, E. Quartarone, P. Mustarelli, I. Rossetti and L. Forni, *Chem. Commun.*, 2007, 5022–5024.

7   G. L. Chiarello, C. Tealdi, P. Mustarelli and E. Selli, *Materials (Basel).*, 2016, **9**, 279.

8   C. Acar and I. Dincer, *Int. J. Hydrogen Energy*, 2016, **41**, 7950–7959.

9   C. A. Bignozzi, S. Caramori, V. Cristino, R. Argazzi, L. Meda and A. Tacca, *Chem. Soc. Rev.*, 2013, **42**, 2228–2246.

10   Y. Xu and M. A. A. Schoonen, *Am. Mineral.*, 2000, **85**, 543–556.

11   H. Zheng, J. Z. Ou, M. S. Strano, R. B. Kaner, A. Mitchell and K. Kalantar-Zadeh, *Adv. Funct. Mater.*, 2011, **21**, 2175–2196.

12   M. Zhang, C. Yang, W. Pu, Y. Tan, K. Yang and J. Zhang, *Electrochim. Acta*, 2014, **148**, 180–186.

13   L. Xia, J. Bai, J. Li, Q. Zeng, X. Li and B. Zhou, *Appl. Catal. B Environ.*, 2016, **183**, 224–230.

14   J. Zhang, Z. Liu and Z. Liu, *ACS Appl. Mater. Interfaces*, 2016, **8**, 9684–9691.

15   J. Zhang, H. Ma and Z. Liu, *Appl. Catal. B Environ.*, 2017, **201**, 84–91.

16   I. Grigioni, K. G. Stamplecoskie, E. Selli and P. V. Kamat, *J. Phys. Chem. C*, 2015, **119**, 20792–20800.

17   W. Kim, T. Tachikawa, D. Monllor-Satoca, H. Kim, T. Majima and W. Choi, *Energy Environ. Sci.*, 2013, **6**, 3732.

18   H. Qi, J. Wolfe, D. Wang, H. J. Fan, D. Fichou and Z. Chen, *Nanoscale*, 2014, **6**, 13457–62.

19   P. J. Kelly and R. D. Arnell, *Vacuum*, 2000, **56**, 159–172.

20   Y. Yamada, K. Tabata and T. Yashima, *Sol. Energy Mater. Sol. Cells*, 2007, **91**, 29–37.

21   V. S. Vidyarthi, M. Hofmann, A. Savan, K. Sliozberg, D. König, R. Beranek, W. Schuhmann and A. Ludwig, *Int. J. Hydrogen Energy*, 2011, **36**, 4724–4731.

22   B. Cole, B. Marsen, E. Miller, Y. Yan, B. To, K. Jones and M. Al-Jassim, *J. Phys. Chem. C*, 2008, **112**, 5213–5220.

23   B. Marsen, E. L. Miller, D. Paluselli and R. E. Rocheleau, *Int. J. Hydrogen Energy*, 2007, **32**, 1310–1315.

24   M. Pedroni, M. Canetti, G. L. Chiarello, A. Cremona, F. Inzoli, S. Luzzati, S. M. Pietralunga,

A. Tagliaferri, M. Zani and E. Vassallo, *Thin Solid Films*, 2016, **616**, 375–380.

25   T. Karabacak, C. R. Picu, J. J. Senkevich, G.-C. Wang and T.-M. Lu, *J. Appl. Phys.*, 2004, **96**, 5740–5746.

26   E. Vassallo, R. Caniello, M. Canetti, D. Dellasega and M. Passoni, *Thin Solid Films*, 2014, **558**, 189–193.

27   G. Bräuer, B. Szyszka, M. Vergöhl and R. Bandorf, *Vacuum*, 2010, **84**, 1354–1359.

28   S. Trasatti and O. A. Petrii, *Pure Appl. Chem.*, 1991, **63**, 711–734.

29   X. Feng, Y. Chen, Z. Qin, M. Wang and L. Guo, *ACS Appl. Mater. Interfaces*, 2016, **8**, 18089–18096.

30   R. Beranek, *Adv. Phys. Chem.*, 2011, **2011**, 80–83.

31   S. P. Harrington and T. M. Devine, *J. Electrochem. Soc.*, 2008, **155**, C381.

32   G. J. Brug, A. L. G. van den Eeden, M. Sluyters-Rehbach and J. H. Sluyters, *J. Electroanal. Chem. Interfacial Electrochem.*, 1984, **176**, 275–295.

33   G. L. Chiarello, A. Zuliani, D. Ceresoli, R. Martinazzo and E. Selli, *ACS Catal.*, 2016, **6**, 1345–1353.

34   P. M. Woodward, A. W. Sleight and T. Vogt, *J. Phys. Chem. Solids*, 1995, **56**, 1305–1315.

35   E. Cazzanelli, *Solid State Ionics*, 1999, **123**, 67–74.

36   H.-R. Wenk and P. Van Houtte, *Reports Prog. Phys.*, 2004, **67**, 1367–1428.

37   C. C. L. McCrory, S. Jung, J. C. Peters and T. F. Jaramillo, *J. Am. Chem. Soc.*, 2013, **135**, 16977–16987.

38   J. O. Bockris, *J. Electrochem. Soc.*, 1984, **131**, 290.

39   T. Kubo, *J. Electrochem. Soc.*, 1998, **145**, 1729.

40   A. Rougier, F. Portemer, A. Quédé and M. El Marssi, *Appl. Surf. Sci.*, 1999, **153**, 1–9.

41   E. Washizu, A. Yamamoto, Y. Abe, M. Kawamura and K. Sasaki, *Solid State Ionics*, 2003, **165**, 175–180.

42   M. B. Johansson, B. Zietz, G. A. Niklasson and L. Österlund, *J. Appl. Phys.*, 2014, **115**, 213510.

43   K. Hong, J. H. Son, S. Kim, B. H. Koo and J.-L. Lee, *Chem. Commun.*, 2012, **48**, 10606–8.

44   F. Wang, C. Di Valentin and G. Pacchioni, *Phys. Rev. B*, 2011, **84**, 73103.

45   F. Wang, C. Di Valentin and G. Pacchioni, *ChemCatChem*, 2012, **4**, 476–478.

46   F. Wang, C. Di Valentin and G. Pacchioni, *J Phys Chem C*, 2012, **116**, 8901–8909.

47   R. Chatten, A. V Chadwick, A. Rougier and P. J. D. Lindan, *J. Phys. Chem. B*, 2005, **109**, 3146–3156.

48   J. Liqiang, Q. Yichun, W. Baiqi, L. Shudan, J. Baojiang, Y. Libin, F. Wei, F. Honggang and S. Jiazhong, *Sol. Energy Mater. Sol. Cells*, 2006, **90**, 1773–1787.

49   G. D. Gilliland, *Mater. Sci. Eng. R Reports*, 1997, **18**, 99–399.

50   W. Wang, A. Janotti and C. G. Van de Walle, *J. Mater. Chem. C*, 2016, **4**, 6641–6648.

51   S. K. Deb, *Sol. Energy Mater. Sol. Cells*, 2008, **92**, 245–258.

52   C. Di Valentin, F. Wang and G. Pacchioni, *Top. Catal.*, 2013, **56**, 1404–1419.

53   Y. Baek and K. Yong, *J. Phys. Chem. C*, 2007, **111**, 1213–1218.

54   G. Orsini, V. Tricoli, A. W. Brinkman, C. G. Granqvist, B. Jankovic, S. Mentus and T. Siemieniewska, *J. Mater. Chem.*, 2011, **21**, 14530.

55   K. R. Reyes-Gil, C. Wiggenhorn, B. S. Brunschwig and N. S. Lewis, *J. Phys. Chem. C*, 2013, **117**, 14947–14957.

56   C. Santato, M. Ulmann and J. Augustynski, *Adv. Mater.*, 2001, **13**, 511–514.

57   A. Hagfeldt and M. Graetzel, *Chem. Rev.*, 1995, **95**, 49–68.

58   J. Bisquert and V. S. Vikhrenko, *J. Phys. Chem. B*, 2004, **108**, 2313–2322.

59   L. Zhang, R. Dillert, D. Bahnemann and M. Vormoor, *Energy Environ. Sci.*, 2012, **5**, 7491–7507.

60   S. Hilaire, M. J. Suess, N. Kranzlin, K. Bienkowski, R. Solarska, J. Augustynski and M. Niederberger, *J. Mater. Chem. A*, 2014, **2**, 20530–20537.

61   V. Cristino, S. Caramori, R. Argazzi, L. Meda, G. L. Marra and C. A. Bignozzi, *Langmuir*, 2011, **27**, 7276–7284.

62   C. Santato, M. Ulmann and J. Augustynski, *J. Phys. Chem. B*, 2001, **105**, 936–940.

63   V. Cristino, S. Marinello, A. Molinari, S. Caramori, S. Carli, R. Boaretto, R. Argazzi, L. Meda and C. A. Bignozzi, *J. Mater. Chem. A*, 2016, **4**, 2995–3006.

64   D. V. Esposito, J. G. Chen, R. W. Birkmire, Y. Chang and N. Gaillard, *Int. J. Hydrogen Energy*, 2011, **36**, 9632–9644.

65   F. Amano, M. Tian, B. Ohtani and A. Chen, *J. Solid State Electrochem.*, 2012, **16**, 1965–1973.

Table 1. Sputtering deposition time, film thickness (d), electrochemical active surface area (ECSA), band gap energy (E_g), flat band potential (E_{FB}), valence band energy (E_{VB}) and density of donors (N_D) of the investigated WO_3 coatings.

Sample	Dep. time (min)	d (nm) [a]	ECSA (cm²)	E_g (eV) [a]	E_{FB} (V vs SHE) [b]	E_{VB} (eV) [c]	N_D [b] (10^{20} cm⁻³)
1L(1.7 Pa)	179	1002	278.8	2.94	0.29	3.0	1.58
1L(3 Pa)	227	976	326.5	2.82	0.39	3.0	1.34
2L(3+1.7 Pa)	106 + 106	942	292.8	2.80	0.34	3.0	0.80

[a] from UV-vis-NIR DRS, (d calculated using a refractive index of 2.2 for WO_3); [b] from Mott-Schottky plots at pH 7 and 21 °C; [c] from XPS valence band spectra.

Table 2. Results of the XPS analysis of used coatings: oxygen to tungsten atomic ratio, percent of W(V) and percent of oxygen as OH moieties.

Sample	O:W at. ratio	% W(V)	% OH
1L(1.7 Pa)	2.64	9.6	19.0
1L(3 Pa)	2.72	9.2	24.8
2L(3+1.7 Pa)	2.70	11.1	19.8

Table 3. PEC water splitting results in 0.5 M Na_2SO_4 and 1.0 V vs. SCE external bias, under 19.7 mW cm⁻² irradiation. η_F = faradaic efficiency

Sample	production rate, r (µmol h⁻¹)		r_{H_2}/r_{O_2}	η_F
	H_2	O_2		
1L(1.7 Pa)	153.9	63.7	2.4	85.6%
1L(3 Pa)	155.6	72.4	2.2	89.8%
2L(1.7+3Pa)*	178.9	67.7	2.6	80.8%
2L(3+1.7 Pa)	187.6	93.2	2.0	93.3%

*Inverted heterojunction

Table 4. Fitting results of the electrochemical impedance spectra according to a $R_s(QR_{ct})$ equivalent circuit. The charge-transfer resistance ($R_{ct,n}$) and the capacitance (C_n) are normalized per unit electrochemical active surface area (ECSA).

| Sample	R_s (Ω)	R_{ct} (Ω)	$R_{ct,n}$ (kΩ cm²)	C_n (µF cm⁻²) [a]
1L(1.7 Pa)	0.67	139	38.7	5.7
1L(3 Pa)	0.73	107	34.9	4.7
2L(3+1.7 Pa)	1.03	86	25.2	5.3
2L(1.7 +3Pa)*	0.98	121	34.0	4.1
1L_calc	0.63	279	4.04	28

[a] Calculated as $C = Y_0^{1/\alpha}(R_s^{-1}+R_{ct}^{-1})^{(\alpha-1)/\alpha}$ from the constant phase element Q of the impedance $Z_Q = Y_0^{-1}(j\omega)^{-\alpha}$, where ω is the angular frequency.

Table 5. Effect of methanol addition on the photocurrent density in linear voltammetry at 1.0 V *vs.* SCE of the investigated samples in comparison to literature data.

Sample [ref]	Electrolite	photocurrent density (mA cm^{-2})		Photocurrent Ratio
		without methanol	with methanol	
1L_calc	0.5 M Na$_2$SO$_4$	1.0	2.4	2.4
1L(3Pa)	0.5 M Na$_2$SO$_4$	1.2	3.9	3.3
2L(3+1.7Pa)	0.5 M Na$_2$SO$_4$	1.6	6.3	3.9
WO$_3$/W anodization[61]	1 M H$_2$SO$_4$	2.9	7.5	2.6
WO$_3$/FTO sol-gel[62]	1 M HClO$_4$	2.4	4.6	1.9
WO$_3$/FTO Colloidal[63]	0.1 M H$_2$SO$_4$	1.3	3.1	2.4
WO$_3$/FTO Colloidal[63]	0.1 M TBAHSO$_4$	2.2	3.0	1.4
WO$_3$/FTO Sputtering[64]	0.33 M H$_2$SO$_4$	2.0	3.5	1.8
WO$_3$/W Hydrothermal[65]	0.1 M H$_2$SO$_4$	3.1	6.5	2.1
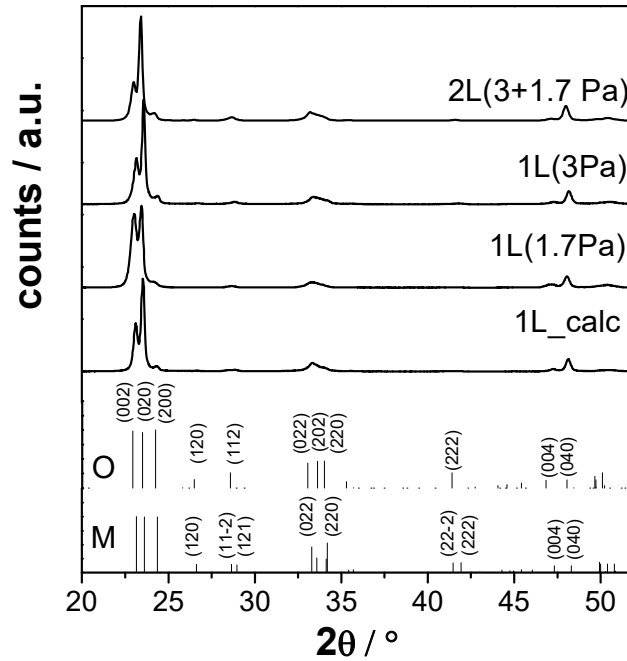
Fig. 1 XRD patterns of the calcined tungsten foil (1L_calc) and of the WO₃ coatings (single and double layers) prepared by RF sputtering and calcined at 600 °C for 2 h. The reflection position and relative intensity of the monoclinic (M) and orthorhombic (O) phases are reported at the bottom of the figure for comparison.
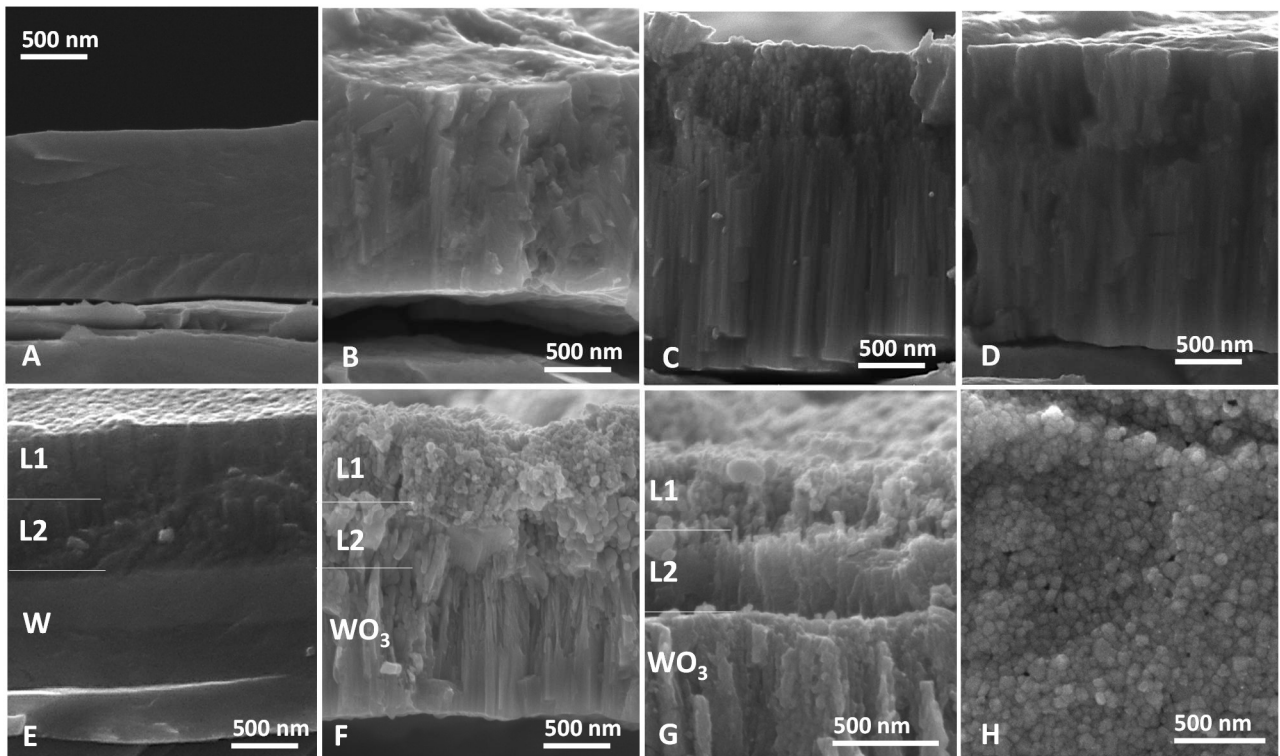
Fig. 2 Cross-section SEM images of (A) the pristine metal tungsten foil and (B) after calcination at 600 °C; (C) 1L(3Pa); (D) 1L(1.7Pa); 2L(3+1.7Pa) (E) before and (F,G) after calcination at 600 °C. (H) Top view of 2L(3+1.7Pa).
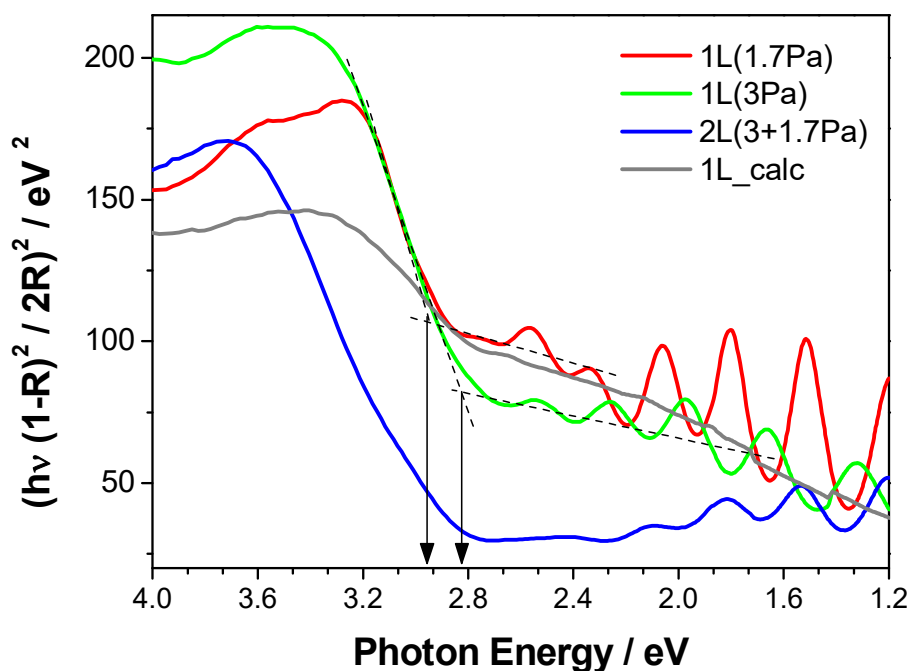
Fig. 3 Tauc plot of the Kubelka-Munk transform UV-vis-NIR diffuse reflectance spectra in the 310 < λ < 1030 nm region and optical band gap determination (allowed direct transition). Spectra recorded on the samples after the 6 h-long photocatalytic water splitting test.
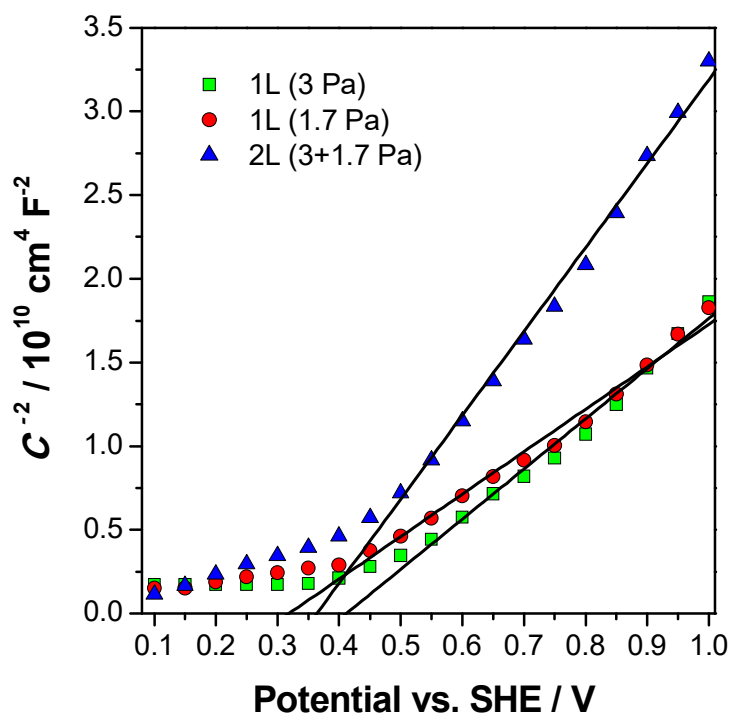
Fig. 4 Mott-Schottky plot measured in 0.5 M Na_2SO_4 (pH 7, at 21 °C) with the investigated sputtered coatings after the 6 h-long photocatalytic water splitting test. The intercept of the straight line with the x-axis corresponds to the $E_{FB} + kT/q$.
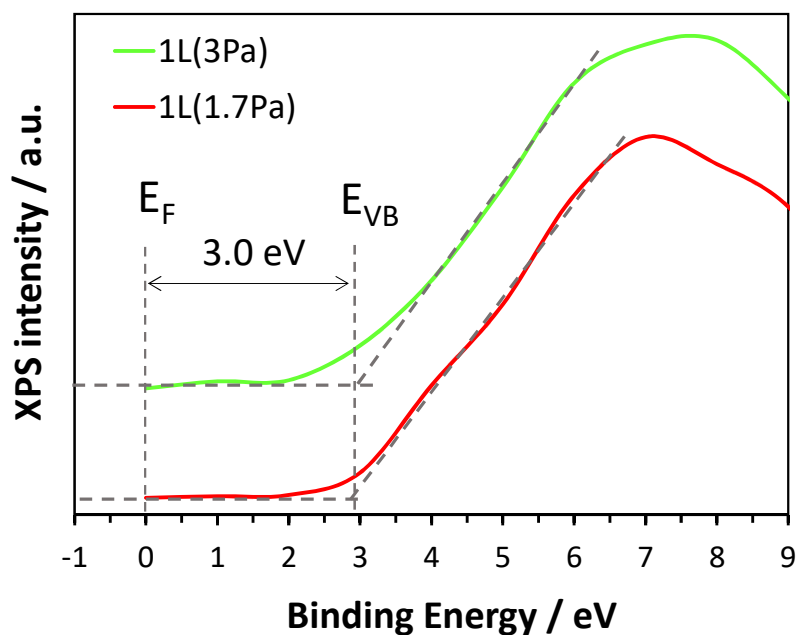
Fig. 5 XPS valence band (VB) spectra of the two monolayer samples. The energy of the VB (E_{VB}) edge is related to the Fermi level (E_F) located at 0 eV.
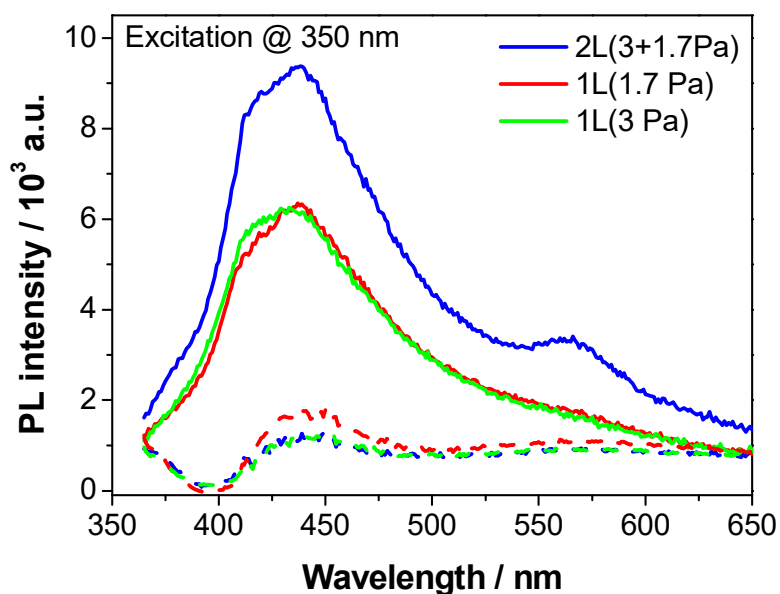
Fig. 6 Comparison of PL spectra (in air, λ_{exc}=350 nm) of the investigated WO_3 sputtered coatings before (solid line) and after (dotted line) the 6 h-long photocatalytic water splitting test.
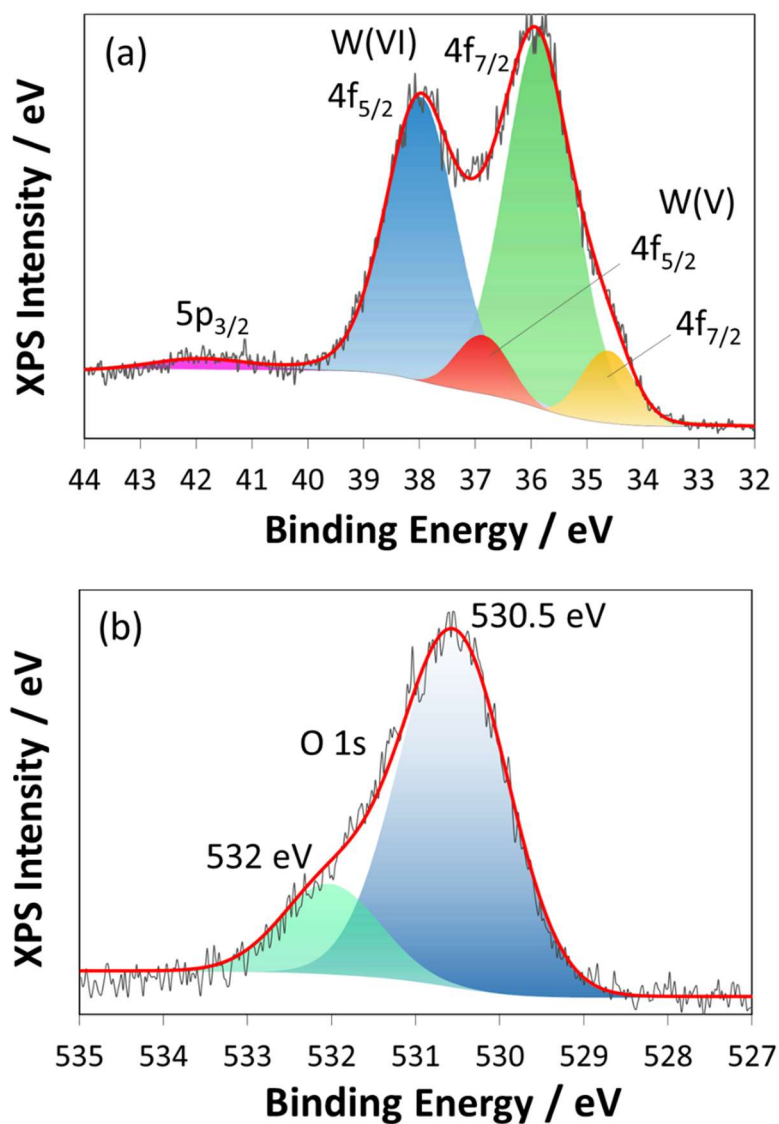
Fig. 7 Experimental (grey line) and fitted (red line) XPS spectra of the used 2L(3+1.7Pa) sample (*i.e.* measured after the 12 h-long irradiation water splitting test) in the (a) W 4f and (b) O 1s binding energy regions. The fitting was performed using a Shirley background.
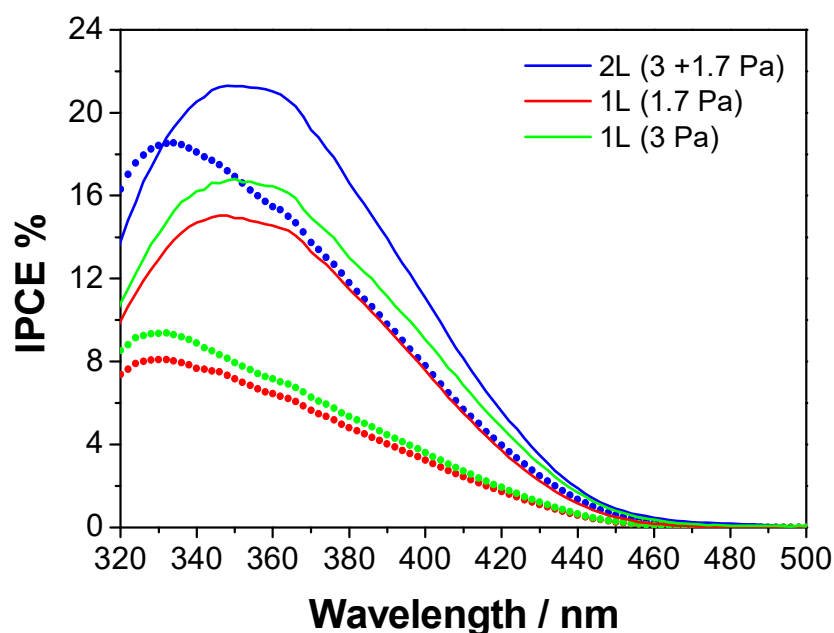
Fig. 8 Incident photon to current efficiency (IPCE) curves of the investigated WO_3 sputtered photoanodes measured at 1.0 V *vs.* SCE in 0.5 M Na_2SO_4, before (dotted line) and after (solid line) the 6 h-long photocatalytic water splitting tests.
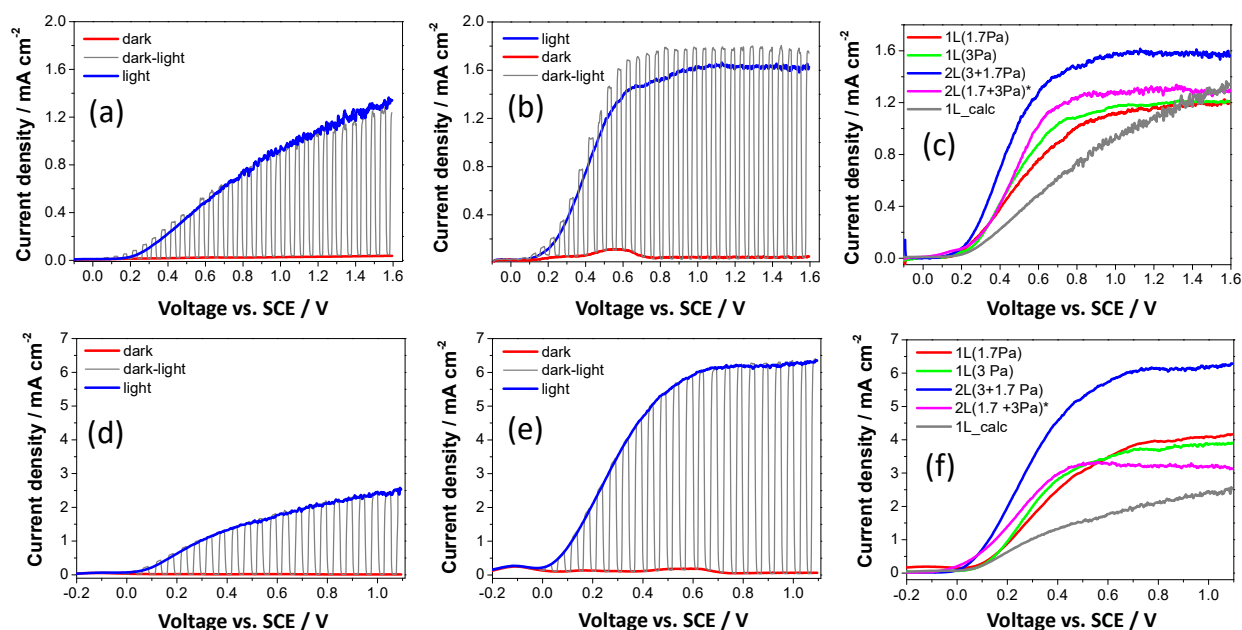

Fig. 9 Polarization curves in (a, b, c) 0.5 M Na_2SO_4 and (d, e, f) 0.5 M Na_2SO_4 + 1.2 M CH_3OH aqueous solution; 9.6 cm^2 photoanode irradiated area, sweep rate 5 mV/s, recorded with the (a, d) 1L_calc WO_3 and (b, e) 2L(3+1.7Pa) photoanodes in the dark (red line); chopped light irradiation with 10 s light/dark cycles (grey line), and full irradiation (blue curve). (c, f) Photocurrent density curves measured under full irradiation with all investigated photoanodes. All measurements were performed on used photoanodes (*i.e.* after the 6 h-long photocatalytic water splitting tests). *Inverted heterojunction.
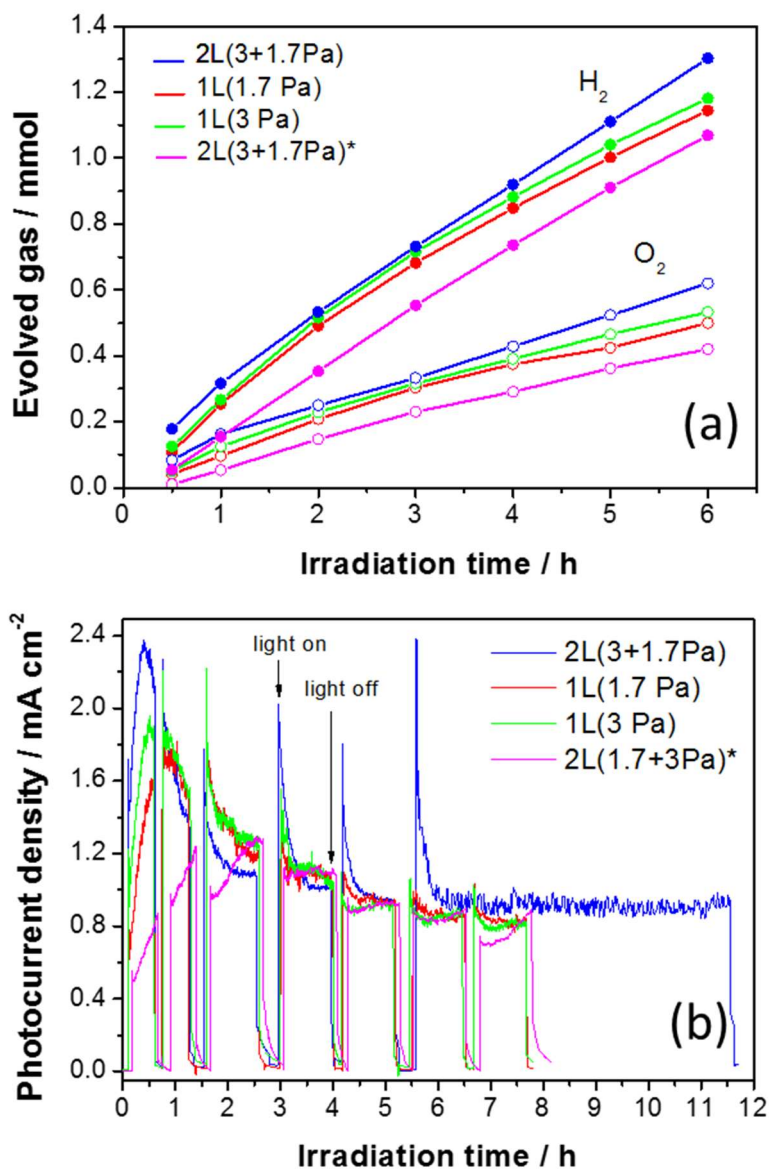
Fig. 10 Photocatalytic water splitting results obtained with the sputtered WO_3 photoanodes in 0.5 M Na_2SO_4 at 1.0 V *vs.* SCE and 9.6 cm^2 irradiated area. (a) Cumulative H_2 and O_2 gas evolution, (b) photocurrent density *vs.* time recorded during the tests. During the evolved gas measurement the light was shuttered causing the photocurrent drop. *Inverted heterojunction.
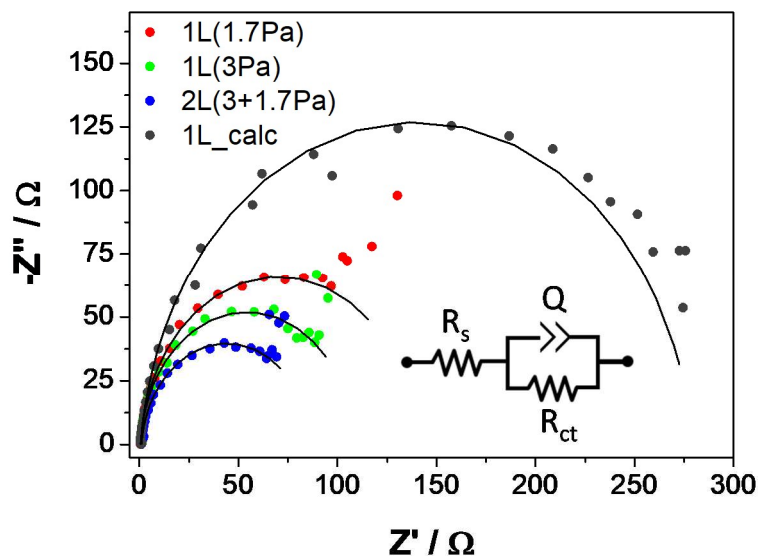
Fig. 11 Nyquist plots of the investigated photoanodes under 1.0 V *vs.* SCE potential in 0.5 M Na_2SO_4 under full lamp illumination. Experimental points (dots) fitted (solid line) by a $R_s(QR_{ct})$ equivalent circuit (inset).
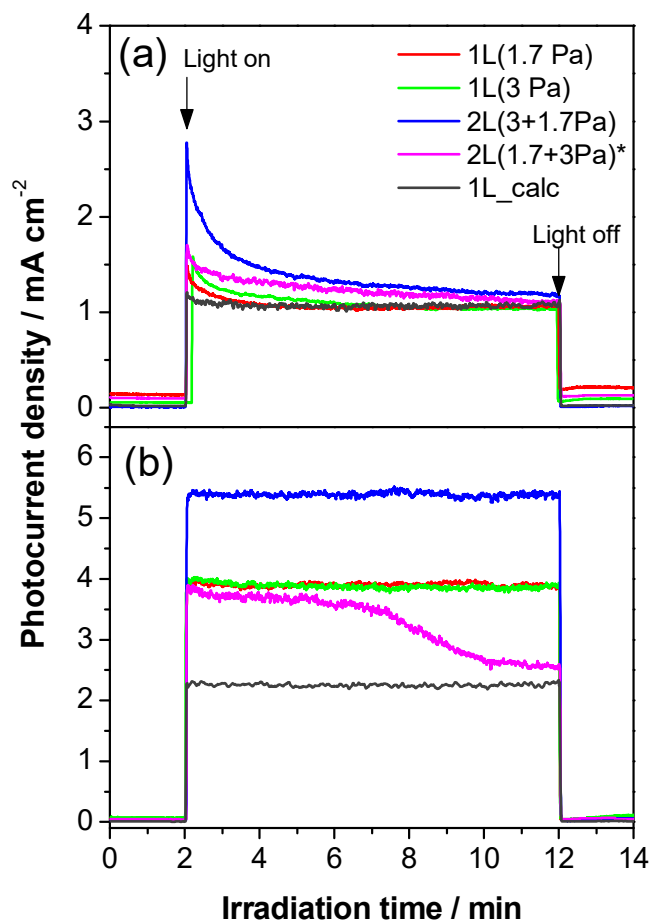
Fig. 12 Photocurrent density response under full lamp irradiation (9.6 cm^2 irradiated area), at 1.0 V *vs.* SCE of used photoanodes in (a) 0.5 M Na_2SO_4 and (b) 0.5 M Na_2SO_4 + 1.2 M CH_3OH. *Inverted heterojunction.
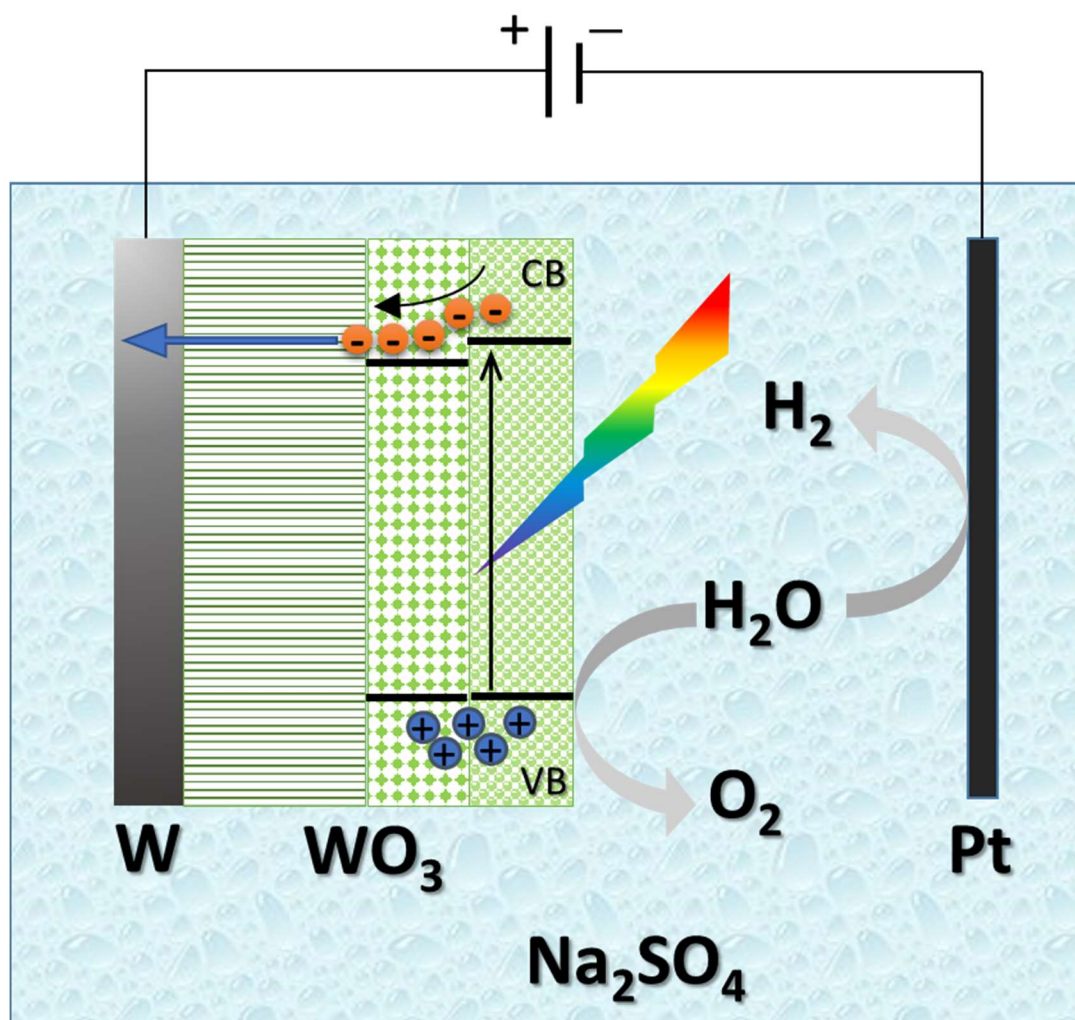
Scheme 1: Schematic representation of the enhanced photopromoted electrons transfer at the sputtered WO_3 bilayer interface due to the formation of the n-n heterojunction.